Materials Science and Engineering A 527 (2010) 3450–3463

Contents lists available at ScienceDirect

Materials Science and Engineering A

journal homepage: www.elsevier.com/locate/msea

# Orientation dependent slip and twinning during compression and tension of strongly textured magnesium AZ31 alloy

T. Al-Samman[a,*], X. Li[a], S. Ghosh Chowdhury[b]

[a] Institut für Metallkunde und Metallphysik, RWTH Aachen, Kopernikusstr. 14, D-52064 Aachen, Germany
[b] CSIR National Metallurgical Laboratory, MST Division, Jamshedpur 831007, India

ARTICLE INFO

*Article history:*
Received 23 November 2009
Received in revised form 1 February 2010
Accepted 2 February 2010

*Keywords:*
Texture
Slip
Twinning
Plastic deformation
DRX

ABSTRACT

Over recent years there have been a remarkable number of studies dealing with compression of magnesium. A literature search, however, shows a noticeably less number of papers concerned with tension and a very few papers comparing both modes, systematically, in one study. The current investigation reports the anisotropic deformation behavior and concomitant texture and microstructure evolution investigated in uniaxial tension and compression tests in two sample directions performed on an extruded commercial magnesium alloy AZ31 at different *Z* conditions. For specimens with the loading direction parallel to the extrusion axis, the tension–compression strength anisotropy was pronounced at high *Z* conditions. Loading at 45° from the extrusion axis yielded a tension–compression strength behavior that was close to isotropic. During tensile loading along the extrusion direction the extrusion texture resists twinning and favors prismatic slip (contrary to compression). This renders the shape change maximum in the basal plane and equal to zero along the *c*-axis, which resulted in the orientation of individual grains remaining virtually intact during all tension tests at different *Z* conditions. For the other investigated sample direction, straining was accommodated along the *c*-axis, which was associated with a lattice rotation, and thus, a change of crystal orientation. Uniaxial compression at a low *Z* condition (400 °C/$10^{-4}$ $s^{-1}$) yielded a desired texture degeneration, which was explained on the basis of a more homogeneous partitioning of slip systems that reduces anisotropy and enhanced dynamic recrystallization (DRX), which counteracts the strong deformation texture. The critical strains for the nucleation of DRX in tensiled specimens at the highest investigated *Z* condition (200 °C/$10^{-2}$ $s^{-1}$) were found to range between 4% and 5.6%.



## 1. Introduction

Typical wrought magnesium alloys (e.g. AZ31, ZK60) exhibit poor room temperature ductility combined with strong mechanical anisotropy, which is attributed to a strong and inadequate texture development during deformation. The stronger the crystallographic texture of a polycrystalline aggregate, the more strongly the single crystal anisotropy manifests itself. In rolled magnesium alloy sheets this typically leads to an undesirable strong in-plane anisotropy, which means that the material yields at a significantly lower stress in compression than in tension [1,2]. This behavior has been attributed to mechanical twinning on the $\{1\,0\,\bar{1}\,2\}$- planes in the $<1\,0\,\bar{1}\,1>$ - directions during compression (*c*-axis extension), but not during tension (*c*-axis compression), owing to the unidirectional nature of mechanical twinning [3–5]. In rolled magnesium sheets twinning is also responsible for the rapid and nearly sudden development of basal texture components during incipient stages of deformation, owing to its 86° $<1\,1\,\bar{2}\,0>$ - crystallographic reorientation of non-basal grains. A basal texture is considered inadequate for deformation, because it places most grains in an orientation difficult to deform, i.e. *c*-axis compression, where the resolved shear stress in the basal plane is practically zero. This results in stress concentration and premature failure [6]. Earlier investigations on the cold deformation behavior of strongly textured AZ31 [7] showed that specimens, which underwent massive mechanical twinning during simple channel-die compression tests failed earlier than specimens with a starting texture or microstructure (ultrafine-grained), designed to inhibit mechanical twinning.

The adoption of designed textures and microstructures in the starting condition of a material undergoing plastic deformation has been proven useful in controlling the texture development. The current study investigates the mechanical response and concomitant texture and microstructure development in a commercially extruded magnesium alloy AZ31 subjected to two contrasting deformation modes; uniaxial compression and tension, respectively. To widen the range of our investigations and explore a variety of deformation scenarios, two specimen orientations were used. Each starting orientation leads to the activation of different

* Corresponding author. Tel.: +49 241 80 26871; fax: +49 241 80 22871.
*E-mail address:* al-samman@imm.rwth-aachen.de (T. Al-Samman).

0921-5093/$ – see front matter © 2010 Elsevier B.V. All rights reserved.
doi:10.1016/j.msea.2010.02.008

slip and twinning systems, and hence, results in a different plastic deformation behavior. The reported results and following discussion are concerned with (a) the effect of loading mode, starting orientation and deformation conditions (temperature and strain rate) on the active deformation mechanisms and dynamic recrystallization (DRX), and (b) the effect of slip and mechanical twinning on the texture development and the resulting flow behavior for each case.

## 2. Experimental procedure

The material investigated was commercially extruded magnesium alloy AZ31 with the following chemical composition (wt.%): 2.90 Al, 0.84 Zn, 0.33 Mn, 0.02 Si, 0.004 Fe, 0.001 Cu, 0.001 Ni, Mg (balance). In order to obtain different starting textures, round tension and compression specimens were machined in two different directions from the extruded material and grouped into two sets; LDED and LD45ED, based on their initial texture (Fig. 1a). The axis of the first set of specimens (labeled as the loading direction LD) was parallel to the extrusion direction ED, hence the labeling LDED, which is also parallel to the basal planes in almost all grains. The axis of the second set of samples was 45° inclined to ED, hence the labeling LD45ED, which is also 45° inclined to the basal planes in most of the grains. The dimensions of the cylindrical specimens for the uniaxial compression tests were 25 mm × Ø 15 mm. The dimensions of the tension specimens were 6 mm diameter and 37 mm gauge length. The deformation experiments were carried out at 200 °C and 400 °C, at constant strain rates of $10^{-2}\,s^{-1}$ and $10^{-4}\,s^{-1}$ respectively, covering a wide processing window of hot plastic deformation of magnesium.

The specimens were heated from top and bottom, up to the desired temperature using heating elements built inside of the crosshead of the testing machine. The time required to raise the temperature to the desired value depended on the test temperature and the specimen geometry and ranged between 2 and 6 min followed by 5 min soaking time to establish thermal equilibrium. During the tests, the temperature difference between top and bottom of the specimen did not exceed 1 °C. This was ensured by temperature calibration prior to the tests using an advanced temperature controller (Eurotherm 2704) and three thermocouples set in top, middle, and bottom of the specimen. Hexagonal boron nitride (h-BN) powder was used as a lubricant for (a) minimizing friction between compression sample and crosshead, i.e. minimizing sample barrelling, and (b) rapid dismounting and quenching of tension specimens. During tensile loading the samples were strained to failure, which took place shortly after necking. In compression, the samples were deformed to selected final strains, up to a maximum logarithmic strain of −1.4, at which the texture and microstructure development have reached a stable state. After completion of the tests, all specimens were rapidly quenched in water in order to freeze the microstructure for subsequent investigations. Specimens for optical microscopy were prepared by conventional grinding and diamond polishing, finishing with a colloidal silica solution. Etching was done using acetic picral solution to visualize grains and grain boundaries. For electron backscatter diffraction (EBSD) analysis, selected samples were additionally electro-polished in a 5:3 solution of ethanol and $H_3PO_4$ to achieve a high indexing rate of Kikuchi patterns. X-ray texture measurements and EBSD were performed in the cross section of deformed specimens, perpendicular to the loading axis. In case of tensiled specimens, the examined surface was located 2 mm away from the necked area. For compression, the texture was measured in the center region of the mid-section of compressed specimens, where the distribution of strain and stress is most homogeneous. The texture was determined by measuring incomplete pole figures between $\alpha = 5–75°$ in the back reflection mode using Co-Kα radiation at 35 kV and 28 mA. A set of six measured pole figures [{1 0 $\bar{1}$ 0}, {0 0 0 2}, {1 0 $\bar{1}$ 1}, {1 0 $\bar{1}$ 2}, {1 1 $\bar{2}$ 0}, and {1 0 $\bar{1}$ 3}] was used to calculate the orientation distribution function (ODF) using MTEX toolbox [8]. Because the uniaxial deformation geometry introduces cylindrical

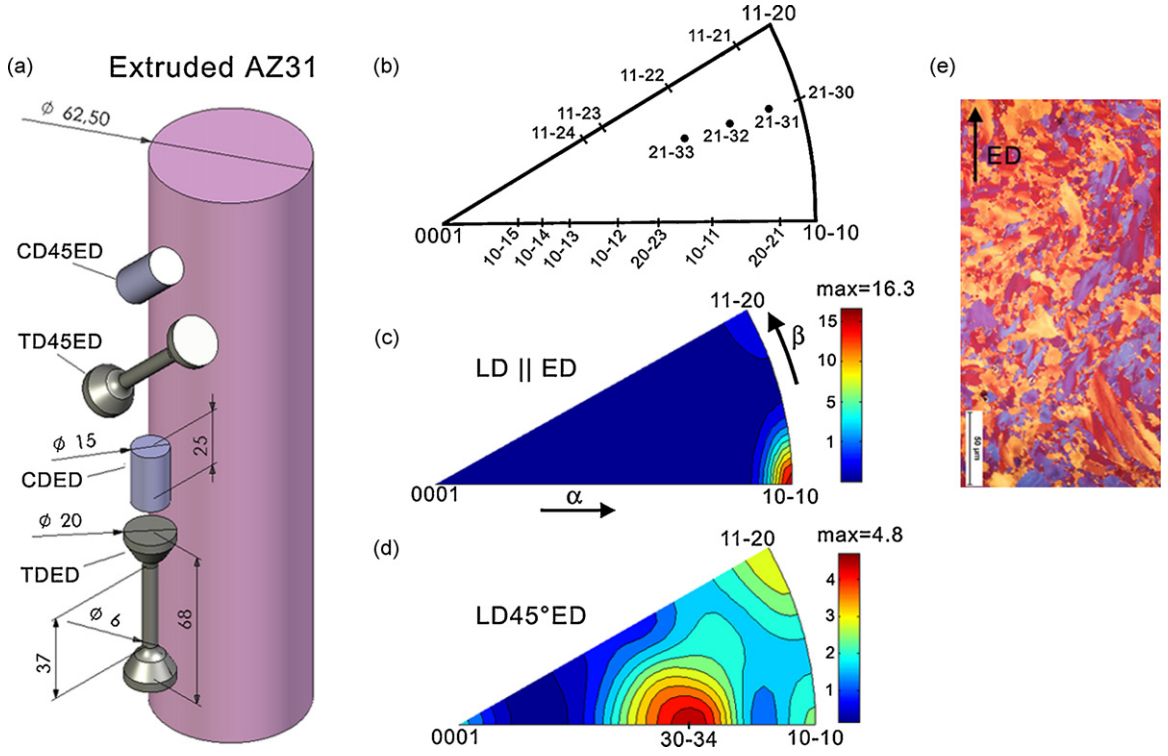


**Fig. 1.** (a) Schematic showing the orientations of compression and tension specimens used in deformation tests. (b) Magnesium unit triangle showing the locations of all major poles. (c) and (d) Measured inverse pole figures showing the initial texture of both specimen types parallel to and 45° inclined to the extrusion axis ED, respectively. LD, loading direction. (e) Initial extrusion microstructure.

sample symmetry it creates certain difficulties with respect to texture representation, i.e. it conceals orientation changes with crystal rotations about the cylinder axis. Therefore, instead of using recalculated pole figures with one defined sample axis (compression direction; CD or tension direction; TD) inverse pole figures (IPF) were adopted for texture representation. Fig. 1b is a standard triangle for magnesium showing normals to crystallographic planes plotted as poles [9]. All major poles are labeled. The positions of poles in the IPF can be determined from straightforward calculations applying the $c/a$ ratio for magnesium ($c/a = 1.624$). For example, the angle (0 0 0 1): $(1\,0\,\bar{1}\,2) = \tan^{-1}(c/a\sqrt{3}) = 43.2^\circ$ and the angle (0 0 0 1): $(1\,0\,\bar{1}\,1) = \tan^{-1}(2c/a\sqrt{3}) = 61.9^\circ$.

## 3. Results

### 3.1. Initial condition

The initial texture and microstructure of the investigated material are shown in Fig. 1. For specimens obtained with their cylinder axis parallel to the extrusion direction, the sharp extrusion texture was familiar for standard magnesium alloys, with basal planes of the hexagonal structure distributed favorably parallel to the extrusion direction ED. From Fig. 1c this can be described as a $< 10\bar{1}0 >$ ED fiber texture. In terms of active deformation mechanisms, this starting orientation is favorable for both dislocation slip and mechanical twinning. Predominance of either slip or twinning responsible for the plastic flow depends strongly on the deformation mode, whether it is tension or compression, and also on the deformation conditions ($T$ and $\dot{\varepsilon}$). For the second set of samples (machined by 45° from the extrusion axis), Fig. 1d shows that the main texture component has the $c$-axis of most of the grains distributed away from the extrusion direction at ($\alpha = 57^\circ$, $\beta = 0^\circ$) ($\alpha$: radial angle, $\beta$: azimuthal angle). This orientation is commonly described as a "soft" orientation that is favorable for easy slip modes (i.e. for slip systems with <$a$> slip vector and low critical resolved shear stress (CRSS), such as basal slip) in both tensile and compressive loading. The extrusion microstructure shown in Fig. 1e comprises coarse deformed grains ($d \sim 20$–$50\,\mu m$) surrounded by fine equiaxed grain structures ($d < 10\,\mu m$). Second phase platelets of $Mg_{17}Al_{12}$ were not present, which means no interference of slip and twinning by precipitates.

### 3.2. Mechanical response

The mechanical response of both specimen sets during tension and compression at different temperatures and strain rates is shown in Fig. 2 by means of stress–strain curves. Although mechanical testing in compression was carried out up to −1.4 logarithmic strain, the flow curves in Fig. 2c and d show selected data up to $\varepsilon = -0.5$ to make comparison with tension more concise. A summary of the numerical data of the conducted tests can be found in Table 1. Since Fig. 2 implicates the influence of several variables (orientation, loading mode, deformation parameters) on the flow behavior, it would be easier to read by noting the following:

(a) Comparison of flow curves within each row (Fig. 2a with Fig. 2b and Fig. 2c with Fig. 2d) demonstrates the influence of texture on

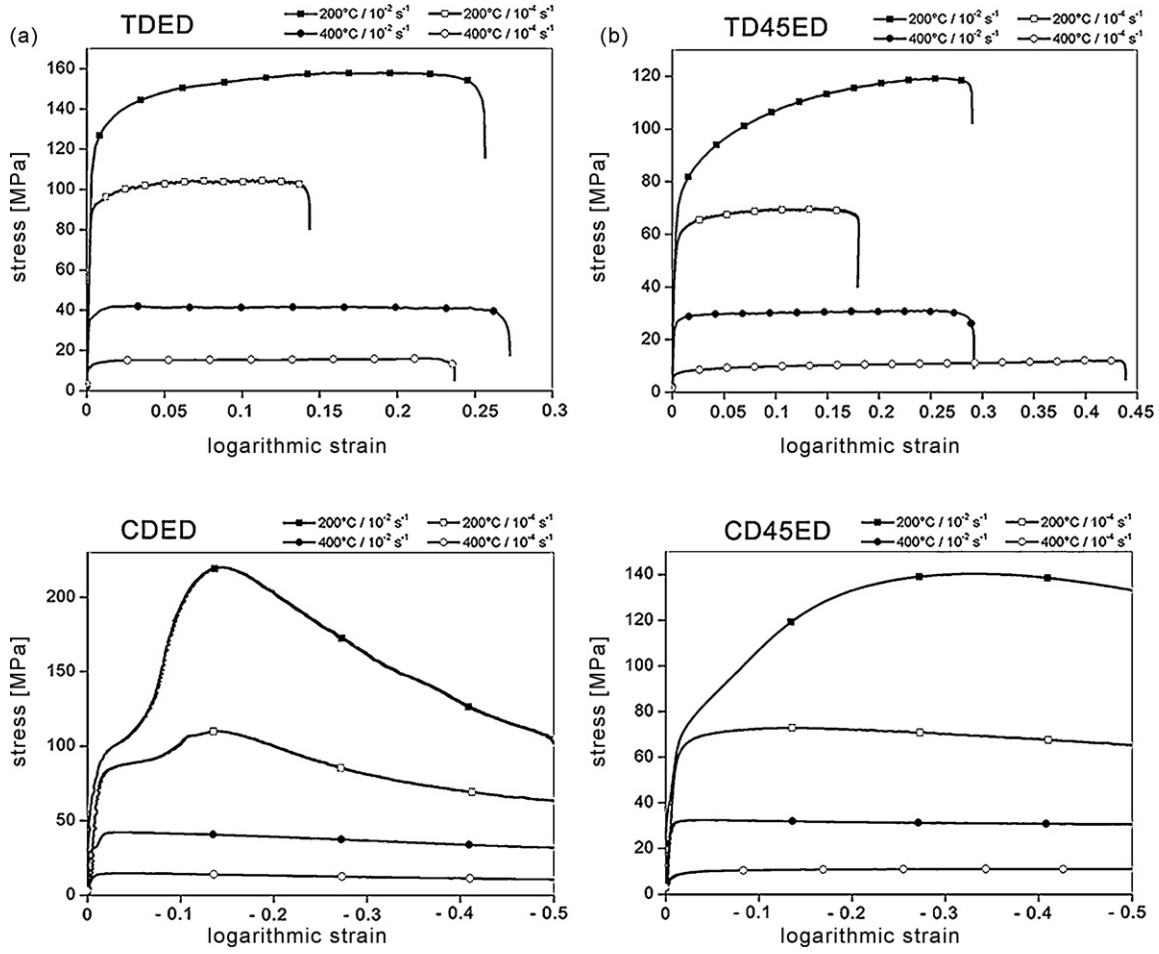


**Fig. 2.** Stress–strain curves of investigated specimen types under various deformation conditions. (a) and (b) for tensile deformation. (c) and (d) for compressive loading.

**Table 1**
Summary of mechanical properties of AZ31 alloy tested in tension and compression at different deformation conditions. $\sigma_y$: yield stress at 0.2% proof strain; $\sigma_p/\varepsilon_p$: peak flow stress and resp. strain; $\varepsilon_f$: failure strain. Stress levels in MPa.

| | Tension | | Compression | |
|---|---|---|---|---|
| | TDED | TD45ED | CDED | CD45ED |
| $\sigma_y$ | | | | |
| 200 °C/$10^{-2}$ $s^{-1}$ | 121 | 60 | 72 | 52 |
| 200 °C/$10^{-4}$ $s^{-1}$ | 92 | 54 | 69 | 44 |
| 400 °C/$10^{-2}$ $s^{-1}$ | 35 | 23 | 28 | 21 |
| 400 °C/$10^{-4}$ $s^{-1}$ | 12 | 6 | 6 | 4 |
| $\sigma_p/\varepsilon_p$ | | | | |
| 200 °C/$10^{-2}$ $s^{-1}$ | 155/0.19 | 116/0.26 | 219/– 0.14 | 140/– 0.33 |
| 200 °C/$10^{-4}$ $s^{-1}$ | 104/0.07 | 69/0.11 | 109/– 0.14 | 72/– 0.11 |
| 400 °C/$10^{-2}$ $s^{-1}$ | 42/– | 31/– | 42/– | 32/– |
| 400 °C/$10^{-4}$ $s^{-1}$ | 15/– | 11/– | 14/– | 11/– |
| $\varepsilon_f$ | | | | |
| 200 °C/$10^{-2}$ $s^{-1}$ | 0.24 | 0.27 | – | – |
| 200 °C/$10^{-4}$ $s^{-1}$ | 0.14 | 0.17 | – | – |
| 400 °C/$10^{-2}$ $s^{-1}$ | 0.26 | 0.28 | – | – |
| 400 °C/$10^{-4}$ $s^{-1}$ | 0.23 | 0.43 | – | – |

strength and ductility (e.g. maximum stress differential in compression, or failure strain differential in tension) for the same loading mode (top row for tension, bottom row for compression).

(b) Comparison within each column (Fig. 2a with Fig. 2c and Fig. 2b with Fig. 2d) reveals the effect of the loading mode in terms of active slip and twinning systems on the flow behavior of the material (flow curve shape and mechanical anisotropy) for the same starting orientation.

(c) Comparison within each individual figure shows the influence of temperature and strain rate, described by the Zener-Hollomon parameter $Z$ ($Z = \dot{\varepsilon}\ \exp\ (Q/RT)$; $Q$: activation energy, $R$: gas constant) on the deformation (e.g. thermal activation of additional deformation mechanisms).

In general, the tension–compression strength anisotropy in typical magnesium alloys is more pronounced under higher $Z$ deformation (lower $T$ and higher $\dot{\varepsilon}$) than during lower ones. For the LDED specimen set deformed at a high $Z$ condition (e.g. 200 °C/$10^{-2}$ $s^{-1}$), the AZ31 material was in terms of yield strength softer in compression than in tension (cf. Fig. 2c and a). However, in terms of work hardening, compression specimens show significantly higher work hardening rate and maximum strength than tension specimens of the same type. The flow curves in compression show a conspicuous peak at $\sigma_p = 219$ MPa, $\varepsilon_p = -0.14$. By contrast, the strain hardening rate in tension was rather low relative to compression, and so was the peak stress (158 MPa), which was obtained at $\varepsilon = 0.19$. The effect of DRX on the flow curve in tension was not as evident as it was in compression (peak flow behavior). This aspect will be pursued further in Section 4. In contrast to LDED specimen group, the strength behavior of LD45ED samples during high $Z$ deformation (e.g. 200 °C/$10^{-2}$ $s^{-1}$ and 200 °C/$10^{-4}$ $s^{-1}$) was surprisingly close to isotropic (cf. Fig. 2b and d).

Fig. 2 reveals that the influence of texture on the work hardening response is much more striking in compression than in tension, which is mainly attributed to mechanical twinning [10,11]. During low $Z$ deformation (e.g. 400 °C/$10^{-2}$ $s^{-1}$ and 400 °C/$10^{-4}$ $s^{-1}$) the anisotropy and strength differential between tension and compression is markedly reduced, most likely owing to (i) more important role of DRX; (ii) thermal activation of <$c+a$>-slip, and (iii) little to no twinning activity.

Fig. 3 compares the tensile fracture of specimens tested at 400 °C (right column) and at room temperature (left column). Note that the ductile failure at 400 °C, by plastic strain localization (necking) (Fig. 3a), is quite different to the abrupt fracture behavior observed at room temperature (shear type failure) (Fig. 3b). Fig. 3c and d is typical SEM images of the corresponding fracture surfaces, taken at low magnification showing the different characteristics of the fracture microstructure.

### 3.3. Deformation textures

The resulting deformation textures of both specimen sets subjected to tensile and compressive loading at various $Z$ conditions show considerable variations in terms of characteristics and sharpness. Since dynamic recrystallization took place during all tests, it is not clear how closely the measured pole figures correspond to the actual deformation texture. Note that the tension and compression textures presented in Figs. 4–7 were measured at different strain levels (at $\varepsilon_f$ for tension and at $\varepsilon = -1.4$ for compression), hence, in some aspects one has to be careful when comparing these textures.

#### 3.3.1. TDED specimens

For tension along the extrusion direction ED (Fig. 4), the strong initial orientation $< 1\,0\,\bar{1}\,0 >$ ED remains the major texture component during all four tests at various $Z$ conditions. This behavior is an indication that all grains resist twinning, and deform favorably by prismatic <$a$>-slip, hence, maintaining a prismatic pole peak parallel to the tension direction TD. Although the qualitative texture character remained more or less unaffected (despite changing $Z$), texture strength showed considerable variations with $Z$. At 200 °C/$10^{-2}$ $s^{-1}$, the deformation texture retained its initial sharpness of 17 MRD (MRD: multiples of a random distribution). Interestingly, holding the deformation temperature at 200 °C and decreasing the strain rate from $10^{-2}$ $s^{-1}$ to $10^{-4}$ $s^{-1}$ (not in the same test) results in a significant drop of texture intensity to 11 MRD. The major texture component $< 1\,0\,\bar{1}\,0 >$ TD in Fig. 4b was accompanied by a second – yet weaker – component; $< 1\,1\,\bar{2}\,0 >$ TD. Note, that the two components are related by a 30° crystallographic rotation about <0 0 0 1>, which is commented on later in Section 4.3. At elevated deformation temperature of 400 °C the concentration of $< 1\,0\,\bar{1}\,0 >$ prismatic poles lying parallel to the tensile direction TD remains unchanged. The presence of the recrystallized $< 1\,1\,\bar{2}\,0 >$ TD component in the inverse pole figure forms a continuous spread of prismatic poles at $\alpha = 90°$, from $\beta = 0°$ to $\beta = 30°$ (Fig. 4b–d).

#### 3.3.2. CDED specimens

For compression along ED, the texture development was entirely different from that resulting from tension. Not only the qualitative character of the texture was different, but also the texture strength was considerably lower (cf. Figs. 4 and 5). The strong initial concentration of prismatic poles parallel to ED was entirely replaced by other favorable orientations, indicating different slip and twinning scenarios relative to tension. Fig. 5 is also indicative that for each $Z$ condition, a different deformation texture was developed, which did not happen during tension.

In Fig. 5a and b (compression at 200 °C) it is obvious from the peak of basal poles parallel to the compression direction CD that {1 0 $\bar{1}$ 2}- tensile twinning was an active player during deformation. With the activation of twinning, basal planes, which were essentially aligned parallel to CD undergo large 86° $< 1\,1\,\bar{2}\,0 >$ crystallographic reorientation to become closely aligned with the compression plane (corresponding texture intensities 4–6 MRD). The texture resulting from twinning can also be described as <0 0 0 1> CD texture or basal texture [12]. The axial spread of basal poles away from CD was somewhat similar for both strain rates ($T = 200$ °C); $\alpha = 0$–38°. Fig. 5a and b indicates no remnants of the initial extrusion texture, and hence, it can be assumed that at

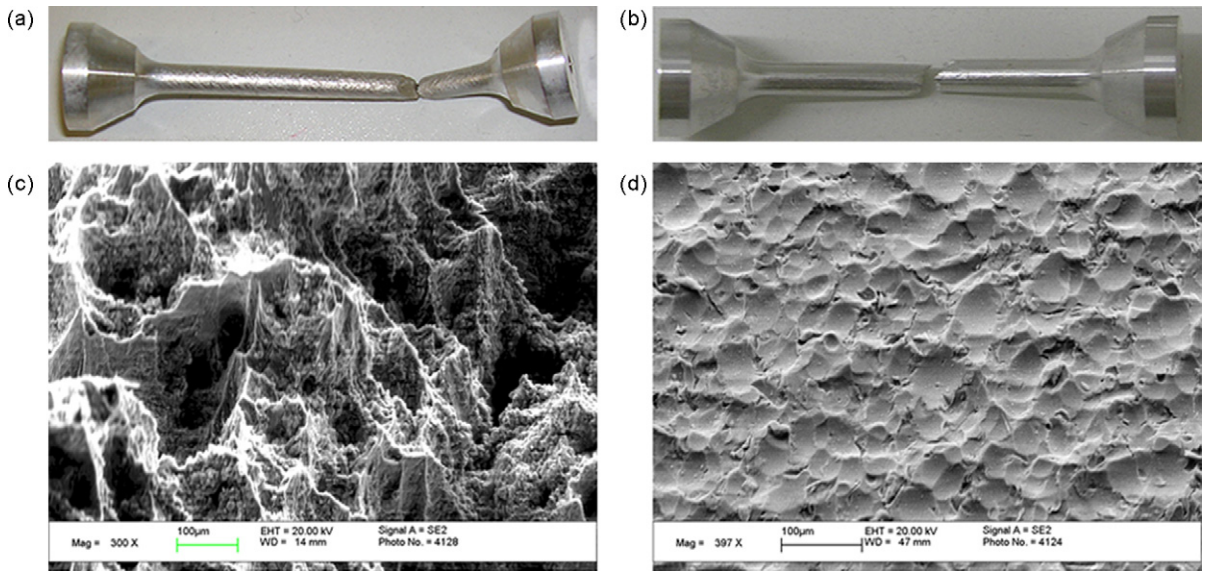


**Fig. 3.** Fracture characteristics and corresponding microstructures of failed specimens tensiled at (a) 400 °C (ductile fracture); (b) at RT (brittle fracture).

200 °C the vast majority of the microstructure underwent twinning. Increasing the deformation temperature to 400 °C seems to markedly influence the compression texture, and the strain rate becomes important. Interestingly, at 400 °C/$10^{-2}$ $s^{-1}$ development of basal texture was suppressed. The main component of the resulting compression texture was located ~20° away from the basal orientation <0 0 0 1> CD, showing a continuous spread between $\beta = 0$ and 7° (Fig. 5c). Lowest *Z* compression at 400 °C/$10^{-4}$ $s^{-1}$ renders the texture virtually random. There is almost no preferred orientation to the loading direction, and the two depicted peaks in the inverse pole figure at ($\alpha = 38°$, $\beta = 0°$) and ($\alpha = 90°$, $\beta = 30°$) are of poor intensity, barely reaching 1.6 MRD.

### 3.3.3. *TD45ED specimens*

For tension at 45° from ED, the measured textures at various deformation conditions show little difference to the initial orientation prior to the tests (Fig. 1d). The initial texture comprised three well-defined orientations; $< 3\,0\,\bar{3}\,4 >$ ED, $< 1\,0\,\bar{1}\,0 >$ ED and $< 1\,1\,\bar{2}\,0 >$ *ED*, which were more or less evident after the deformation (with some scatter). The resulting tension orientations; $< 1\,0\,\bar{1}\,1 >$ *TD* (Fig. 6a) and $< 4\,0\,\bar{4}\,5 >$ *TD*, (Fig. 6b–d) were located between <0 0 0 1> and $< 1\,0\,\bar{1}\,0 >$ poles with little $\alpha$ variations relative to each other, and to the starting orientation $< 3\,0\,\bar{3}\,4 >$ *ED*. This is indicative of basal slip activity as discussed later. With respect to the other components of the texture, Fig. 6a indicates that the $< 1\,0\,\bar{1}\,0 >$ *TD* orientation was markedly the strongest after tension at 200 °C/$10^{-2}$ $s^{-1}$ (highest *Z* condition), whereas the $< 1\,1\,\bar{2}\,0 >$ TD orientation was most evident after tension at 400 °C/$10^{-4}$ $s^{-1}$ (lowest *Z* condition) (Fig. 6d). In the other two *Z* conditions (Fig. 6b and c) these two orientations are of intermediate strength relative to the strongest texture component.

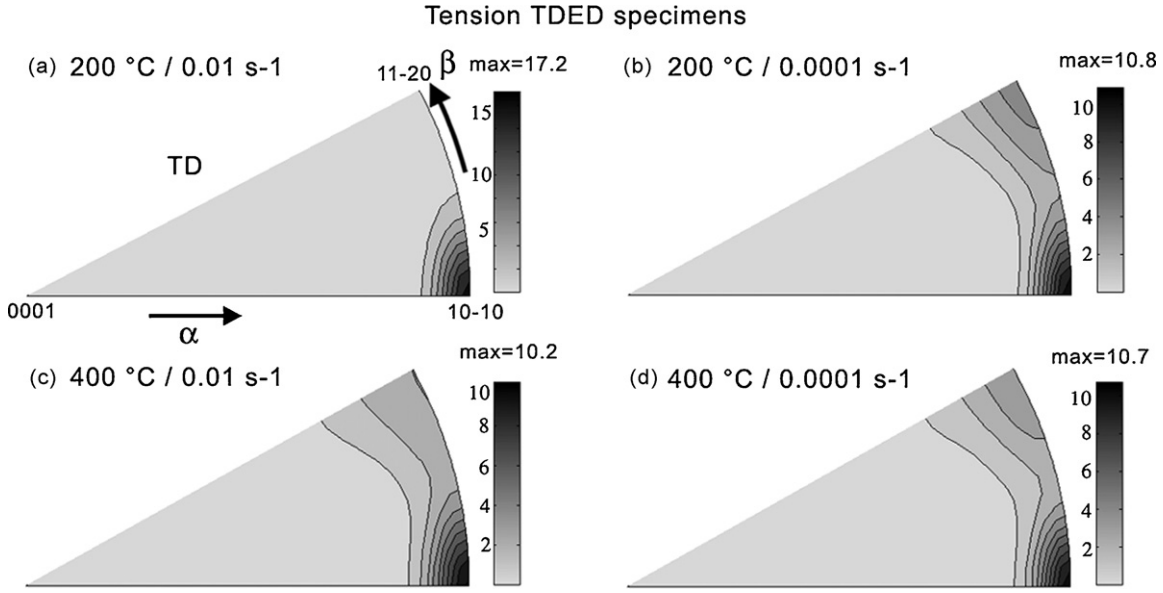


**Fig. 4.** Measured inverse pole figures showing the macroscopic texture development upon tension of TDED specimens to failure at (a) 200 °C/$10^{-2}$ $s^{-1}$; (b) 200 °C/$10^{-4}$ $s^{-1}$; (c) 400 °C/$10^{-2}$ $s^{-1}$; (d) 400 °C/$10^{-4}$ $s^{-1}$. $\alpha$: Radial angle, $\beta$: azimuthal angle. TD, tension direction, i.e. the sample reference direction with respect to the local crystal axes. The scale at right indicates the relative diffraction intensity (1.0 = random).

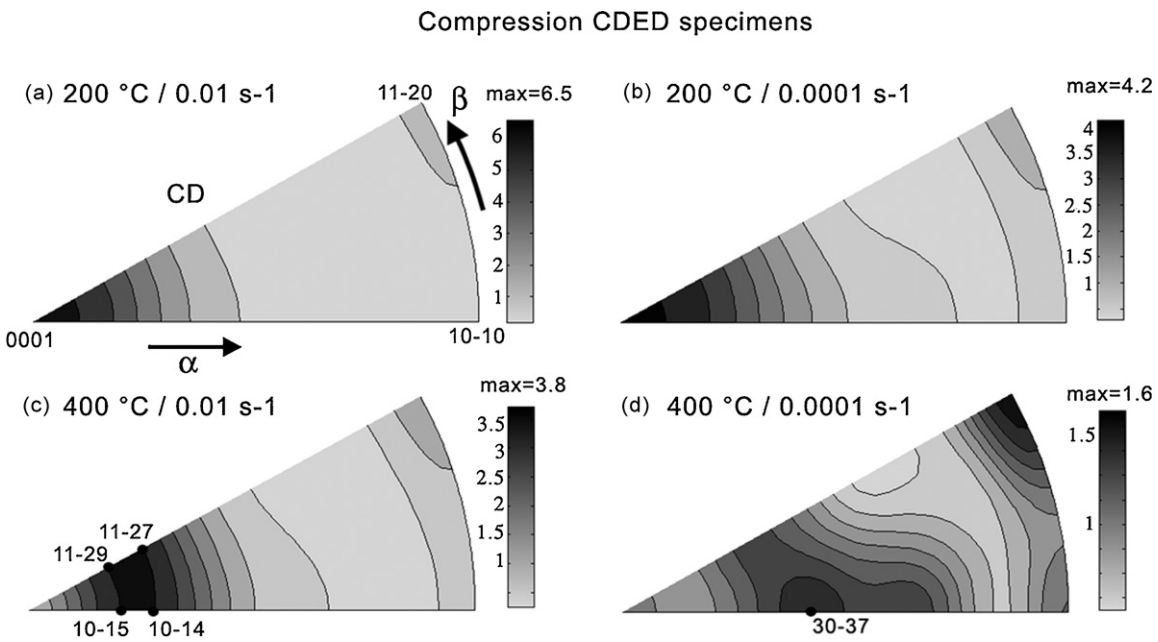


**Fig. 5.** Measured inverse pole figures showing the macroscopic texture development upon compression of CDED specimens to $\varepsilon = -1.4$ at (a) 200 °C/$10^{-2}$ $s^{-1}$; (b) 200 °C/$10^{-4}$ $s^{-1}$; (c) 400 °C/$10^{-2}$ $s^{-1}$; (d) 400 °C/$10^{-4}$ $s^{-1}$. CD: compression direction, i.e. the sample reference direction with respect to the local crystal axes.

### 3.3.4. CD45ED specimens

By contrast to the texture development during tension (Fig. 6), the starting orientation of CD45ED specimens (Fig. 1d) changes significantly when loaded in compression at 45° from the ED (Fig. 7). Unlike in tension, the compression textures of deformed CD45ED specimens show only one orientation, located near to the <0 0 0 1> pole. Its sharpness and scatter from an ideal basal orientation depend on the deformation conditions. Upon the highest $Z$ deformation (200 °C/$10^{-2}$ $s^{-1}$), the $c$-axis in almost all grains was closely aligned with the loading direction, forming a typical basal texture with a maximum intensity of ~7 MRD and a maximum spread of $\alpha = 40°$ (Fig. 7a). With decreasing $Z$ the material becomes less prone to developing a basal orientation, as the strongest intensity shifts away from <0 0 0 1> pole by 10–15° (Fig. 7b–d).

### 3.4. Deformation microstructures

The microstructure of deformed specimens was influenced by (i) the loading mode and (ii) the deformation conditions. The loading type, being tensile or compressive, controlled whether the $c$-axis in grains undergoes contraction or extension, and hence, whether accordingly twinning is activated or not. Typical micrographs are shown in Fig. 8 demonstrating the microstructures consistent with tension and compression after equal deformation of ~25% at 200 °C/$10^{-2}$ $s^{-1}$. While the tension microstructure of failed TDED specimens shows virtually no twins (Fig. 8b), some twinned grains were seen in the compression microstructure of CDED specimens (Fig. 8a). The fraction of twinned material seems somewhat lower than expected even though the initial grain orientation very much

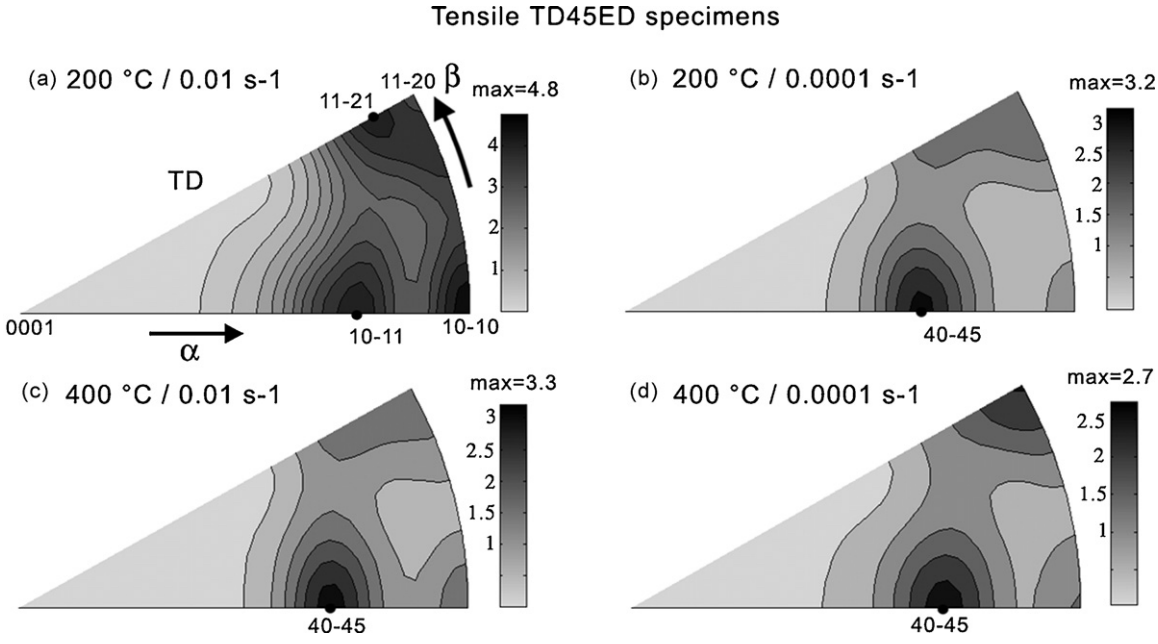


**Fig. 6.** Measured inverse pole figures showing the macroscopic texture development upon tension of TD-45ED specimens to failure at (a) 200 °C/$10^{-2}$ $s^{-1}$; (b) 200 °C/$10^{-4}$ $s^{-1}$; (c) 400 °C/$10^{-2}$ $s^{-1}$; (d) 400 °C/$10^{-4}$ $s^{-1}$.

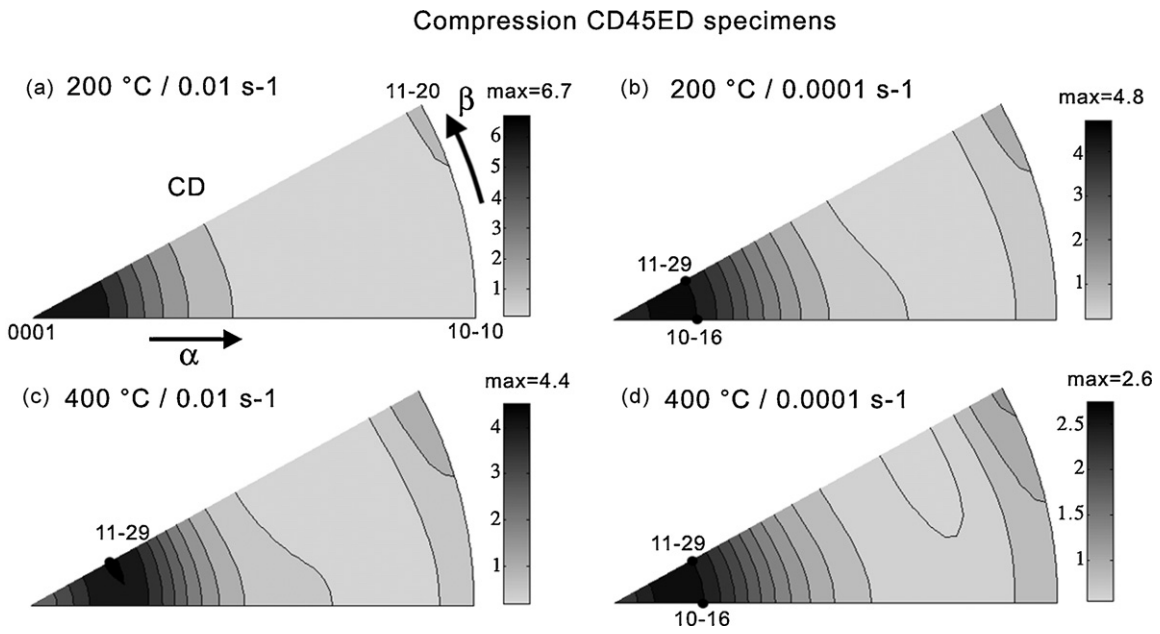


**Fig. 7.** Measured inverse pole figures showing the macroscopic texture development upon compression of CD45ED specimens to $\varepsilon = -1.4$ at (a) 200 °C/$10^{-2}$ $s^{-1}$; (b) 200 °C/$10^{-4}$ $s^{-1}$; (c) 400 °C/$10^{-2}$ $s^{-1}$; (d) 400 °C/$10^{-4}$ $s^{-1}$.

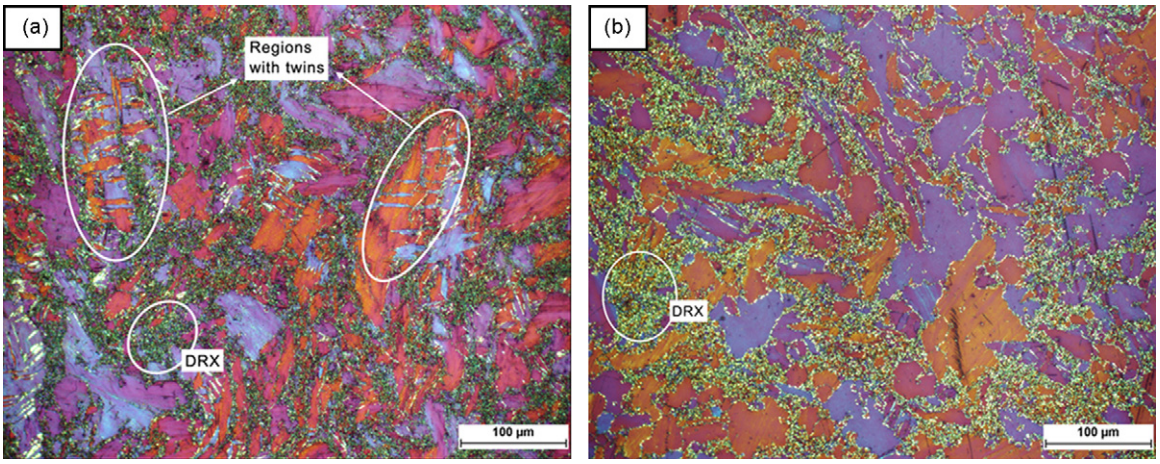


**Fig. 8.** Optical micrographs showing the deformation microstructures of CDED and TDED specimens upon (a) compression to $\varepsilon = -0.2$; (b) tension to failure ($\varepsilon_f \sim -0.2$) at 200 °C/$10^{-2}$ $s^{-1}$. Micrograph plane is perpendicular to the loading axis.

favored $\{1\,0\,\bar{1}\,2\}$- twinning. This observation, however, should not be misinterpreted by the assumption that $\{1\,0\,\bar{1}\,2\}$- twinning had not contributed in a major way as a deformation mechanism. The reason why only a few mechanical twins are seen in Fig. 8a is ascribed to the strain level of −0.25, at which the test in compression was terminated for comparison purposes with tension. Fig. 9 demonstrates the evolution of twin microstructure during compression of CDED specimens at 200 °C/$10^{-2}$ $s^{-1}$ for strains equal to

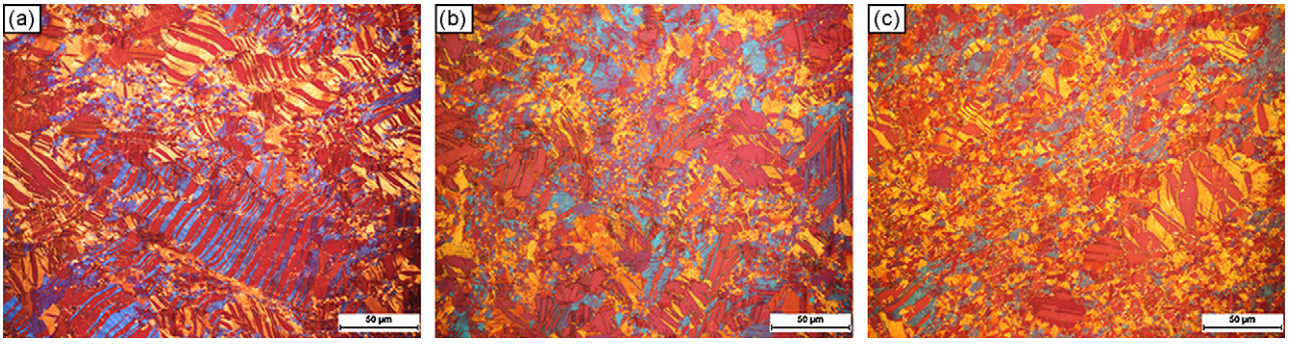


**Fig. 9.** Optical micrographs showing the evolution of twin fraction in the compression microstructure of CDED specimens as a function of strain. (a) $\varepsilon = -0.05$; (b) $\varepsilon = -0.1$; (c) $\varepsilon = -0.15$. $T = 200$ °C, $\dot{\varepsilon} = 10^{-2}$ $s^{-1}$. Micrograph plane is perpendicular to the loading axis.

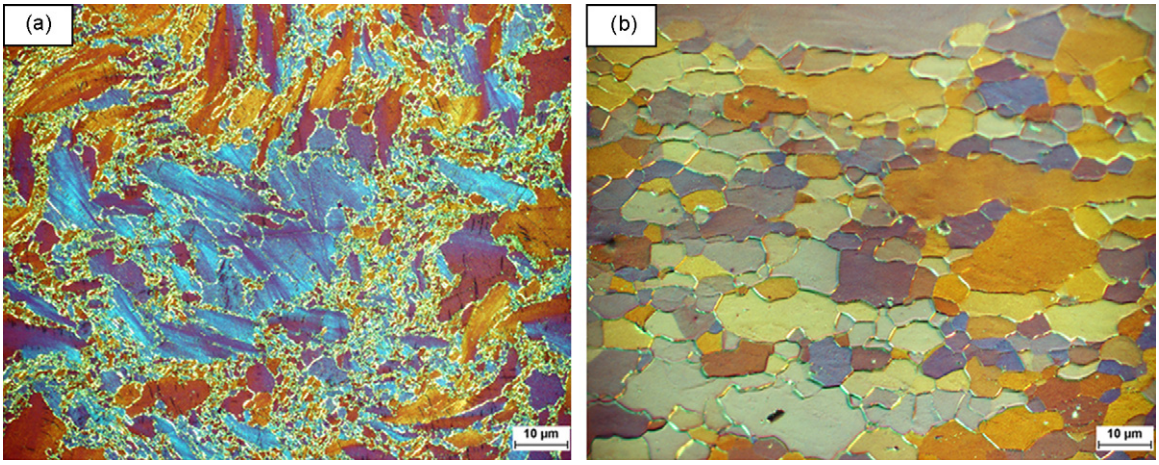


**Fig. 10.** Optical micrographs showing the DRX microstructure (grain size and volume fraction recrystallized) in TD45ED specimens tensiled to failure at (a) 200 °C/$10^{-2}$ $s^{-1}$ and (b) 400 °C/$10^{-4}$ $s^{-1}$. The corresponding strains can be found in Table 1. Micrograph plane is perpendicular to the loading axis.

−0.05, −0.1 and −0.15, respectively. Evidently, profuse twinning is rather observed at lower strain levels, most probably up to ∼0.05% (Fig. 9a). With increasing strain, tensile twinning ceases to operate (owing to its unidirectional nature, i.e. twinned grains cannot twin back when they are still being loaded in compression), and the imposed deformation is mainly accommodated by slip. Additionally, with the onset of DRX, presumably at strains lower than 0.2 the whole microstructure undergoes significant changes, which strongly affect the morphology of preexisting twins. This leads to a decreasing twin fraction with increasing deformation as observed in Fig. 9b and c. It is also to be mentioned here that the twin fraction in magnesium becomes underpredicted at high strain levels, as multiple twins in the microstructure grow and eventually consume entire parent grains, making them indistinguishable from the original matrix. At 400 °C mechanical twinning was rendered unimportant for deformation.

Other microstructural aspects, such as grain size, grain shape and fraction recrystallized were more influenced by the deformation conditions (strain amount, deformation temperature and strain rate) rather than the loading mode. At 200 °C/$10^{-2}$ $s^{-1}$ (highest $Z$ condition) and a corresponding tensile elongation of ∼25% the microstructure of TD45ED shows coarse deformed grains embedded within a fine dynamically recrystallized structure with an average grain size of ∼2 μm (Fig. 10a). At 400 °C/$10^{-4}$ $s^{-1}$ (lowest $Z$ condition) and a corresponding strain of ∼45% the microstructure appears in a fully recrystallized condition with an average grain size of ∼16 μm (Fig. 10b).

## 4. Discussion

### 4.1. Deformation behavior during compression

Crystallographic slip in magnesium occurs most readily parallel to the basal planes. When the material is compressed along the extrusion axis, as is the case of CDED texture type (Fig. 1c), the resolved shear stress on the basal planes is close to zero, and the stress is accordingly maximized in this condition. However, mechanical twinning is an additional mechanism for plastic deformation in magnesium and the most common twin type $\{1\,0\,\bar{1}\,2\}$ < $1\,0\,\bar{1}\,1$ > (tensile twin) causes extension along the $c$-direction [3–5,10]. Other important slip systems such as prismatic <$a$> slip and second pyramidal <$c+a$> slip may also be activated, if the grains were accordingly favorably oriented, and the corresponding activation stresses were reached. Which deformation mechanism (whether non-basal slip or twinning) will dominate the plastic flow depends mainly on the deformation temperature and strain rate.

At 200 °C tensile twinning is activated when the CDED specimens are subjected to compressive loading, which results in a low yield strength of ∼100 MPa (Fig. 2c). The activity of twinning can be assigned to the small strain regime of the work hardening curve between 0.1% and 6%. At higher strains, twinning is already exhausted (maximum twinning strain for tensile twinning in Mg is about 6.5%), and the stress for continued plastic deformation rises quite strongly with strain, resulting in a second work hardening regime with a lower slope. This behavior can be rationalized in terms of unfavorable grain orientation for deformation after twinning, i.e. $c$-axis compression, which necessitates a significantly higher stress level for the activation of pyramidal <$c+a$> slip. Additionally, slip in twins requires higher stresses to initiate since the dislocation movement within twins is restricted by a much shorter mean free path than in the matrix [11].

Mechanical twinning does not only have a high impact on the hardening response of a deformed material, but also on its texture development [4]. As a consequence of the twinning event, basal planes of twinned grains are typically rotated by 86° from the initial prism orientation (depicted in Fig. 1c) to assume a basal orientation. This large reorientation can be readily observed at a low strain equal to 5% for $T$ = 200 °C and $\dot{\varepsilon} = 10^{-2}$ $s^{-1}$ (Fig. 11a). Since twinning the whole microstructure requires some time, the initial extrusion texture shows three components simultaneously; <0 0 0 1> $CD$, < $1\,0\,\bar{1}\,0$ > CD and < $1\,1\,\bar{2}\,0$ > CD, with corresponding maximum intensities of 21 MRD, 6 MRD and 2 MRD, respectively (Fig. 11a). When the deformation strain reaches 15% under the same $Z$, the entire microstructure is already reoriented into a sharp basal orientation (28 MRD) with markedly low scatter (∼10°) about CD (Fig. 11b). During deformation between 15% and 140% the basal nature of the texture remains more or less unchanged, but the texture sharpness decreases by nearly 75% (cf. Fig. 7a). Moreover, the maximum spread of the $c$-axes about CD increases from 10° at $\varepsilon$ = −0.05 to 30° at $\varepsilon$ = −1.4 (at equal scatter intensity of 2 MRD).

Uniaxial compression has no constraints for plastic deformation in any direction other than the compression direction, and hence, in terms of favorable orientation all grains in CDED specimens can undergo twinning during incipient deformation. From the same Schmid factor (SF) perspective, the whole microstructure could also be deformed by prismatic <$a$> slip or pyramidal <$c+a$> slip (but not by basal slip). At 200 °C the macroscopic stress of the specimen would still be lower than the activation stress of pyramidal <$c+a$> slip, but it is possibly high enough to activate prismatic slip. The results, however, obviously show that twinning, and not prismatic slip, dominates the deformation of CDED specimens at 200 °C under both strain rates $10^{-2}$ $s^{-1}$ and $10^{-4}$ $s^{-1}$.

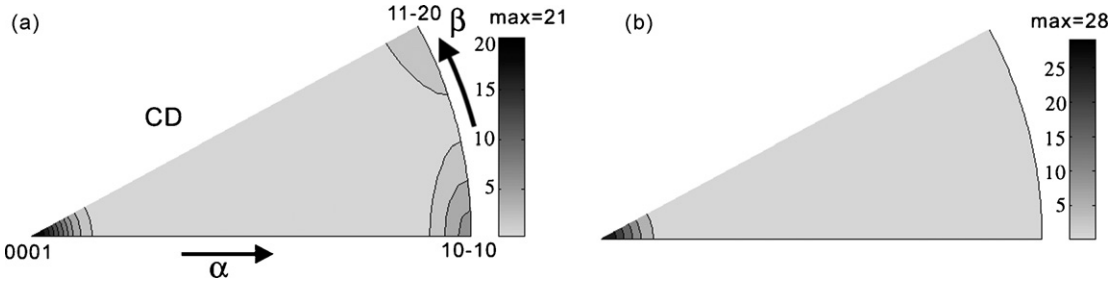


**Fig. 11.** Measured inverse pole figures showing the macroscopic texture development (with respect to tensile twinning) of CDED specimens at selected deformation stages. (a) $\varepsilon = -0.05$; (b) $\varepsilon = -0.15$. Deformation temperature $T = 200\,^{\circ}C$, strain rate $\dot{\varepsilon} = 10^{-2}\,s^{-1}$.

Note that when twinning is already exhausted at early stages of deformation, prismatic slip will not be a deformation contributor, even if the stress level was high enough to initiate it, because with the new grain orientation the resolved shear stress on prismatic planes is practically zero. At this point the deformation has absolutely no means for accommodating the strain along the *c*-axis, so accordingly the material hardens and the flow stress increases rapidly with strain. Before the flow stress in the specimen reaches either one of the fracture stress or the CRSS for pyramidal <*c* + *a*> slip, dynamic recrystallization occurs, reducing the high density of tangled dislocations, thus restoring ductility to the material. DRX manifests itself by the peak stress between hardening and softening regimes in the flow curves at $200\,^{\circ}C/10^{-2}\,s^{-1}$ and $200\,^{\circ}C/10^{-4}\,s^{-1}$ (Fig. 2c).

At temperatures above 200 °C twinning remains to some extent necessary to accommodate the *c*-direction extension. This is seen in the deformation of selected specimens at $300\,^{\circ}C/10^{-2}\,s^{-1}$, where the transformation into a basal texture as a consequence of twinning is almost completed after −15% straining (Fig. 12a). Further increase of the deformation temperature to 400 °C (holding the strain rate at $10^{-2}\,s^{-1}$) renders twinning unimportant for the deformation, and the specimens are more prone to deform by slip instead. This is demonstrated in Fig. 12b, where the initial prismatic orientation remains unaffected after 15% deformation, which is indicative of predominant prismatic slip activity. Depending on whether single or double prismatic slip (i.e. concurrent activation of two prismatic slip systems; e.g. $(0\,1\,\bar{1}\,0)\,[2\,\bar{1}\,\bar{1}\,0]$ and $(1\,\bar{1}\,0\,0)\,[1\,1\,\bar{2}\,0]$ is activated, either $< 1\,1\,\bar{2}\,0 >$ or $< 1\,0\,\bar{1}\,0 >$ slip direction will be aligned with the extension direction perpendicular to the loading axis. Hence, the appearance of an additional $< 1\,1\,\bar{2}\,0 >$ CD component in Fig. 12b can be rationalized on the basis of double prismatic slip activity. Detailed discussion of double prismatic slip in textured magnesium can be found in [13]. Another possible explanation for the $< 1\,1\,\bar{2}\,0 >$ CD component is DRX. Recrystallization is known to promote a 30° <0 0 0 1> rotation during nucleation and growth of recrystallized grains in hexagonal materials [14–16]. With a concept that dynamic recrystallization is a superposition of deformation and static recrystallization, DRX can also be claimed responsible for the development of the $< 1\,1\,\bar{2}\,0 >$ CD component during deformation.

As found earlier, Fig. 12b shows that prismatic slip is a major deformation contributor during compression of CDED specimens at $400\,^{\circ}C/10^{-2}\,s^{-1}$ up to strains of −0.15. With increasing strain, it is, however, proposed that other slip modes take over the deformation, causing a shift in the maximum pole density of the texture in Fig. 5c towards <0 0 0 1> pole (i.e. the *c*-axis in the grains rotates towards the compression direction).

The most interesting texture development – in terms of substantial texture regression – was observed during compression of CDED specimens at $400\,^{\circ}C/10^{-4}\,s^{-1}$ (Fig. 5d), which was tracked in detail as a function of strain (Fig. 13) in order to understand the process. At −0.1 strain, little variation is observed in the initial extrusion texture, which still comprises the two orientations; $< 1\,0\,\bar{1}\,0 >$ CD (being the preferred one) and $< 1\,1\,\bar{2}\,0 >$ CD. The texture intensity shows a drop to 12 MRD, and the deformation occurs mainly by <*a*> slip on prismatic planes (Fig. 13a). At −0.2 deformation, some minor components in the texture spread are rotated away from the preferred prismatic orientation; $< 1\,0\,\bar{1}\,0 >$ CD towards the <0 0 0 1> pole (Fig. 13b). This tendency to alter the texture character readily at −0.2 strain can be attributed to the activation of additional slip systems. In fact there are four $\{1\,\bar{1}\,0\,1\}$ pyramidal planes that are favorably oriented for <*a*> slip in compression besides prismatic planes.

Using $m = (\sqrt{3}/4)h\,(h^2 + (3a^2/4c^2)l^2)^{-1/2}$ [13], the Schmid factor for $\{1\,\bar{1}\,0\,1\} < 1\,1\,\bar{2}\,0 >$ pyramidal slip is found to be equal to 0.38. With the activation of <*a*> pyramidal slip a high proportion of the $< 1\,0\,\bar{1}\,0 >$ CD component is rotated from a prismatic orientation towards pyramidal orientation, associated with a considerable decrease of texture sharpness by approximately 50%. With the development of a pyramidal orientation at ($\alpha = 62°$, $\beta = 0°$) after 30% deformation (Fig. 13c), the resolved shear stress on $\{1\,\bar{1}\,0\,1\}$ pyramidal slip planes becomes practically zero, and hence <*a*> pyramidal slip is rendered inactive. However, the new $< 1\,\bar{1}\,0\,1 >$ CD orientation is favorable for basal slip, more precisely, for double basal slip according to Munroe et al. [17] (Fig. 14). Owing to basal slip, grains with a pyramidal orientation are rotated towards the <0 0 0 1> pole

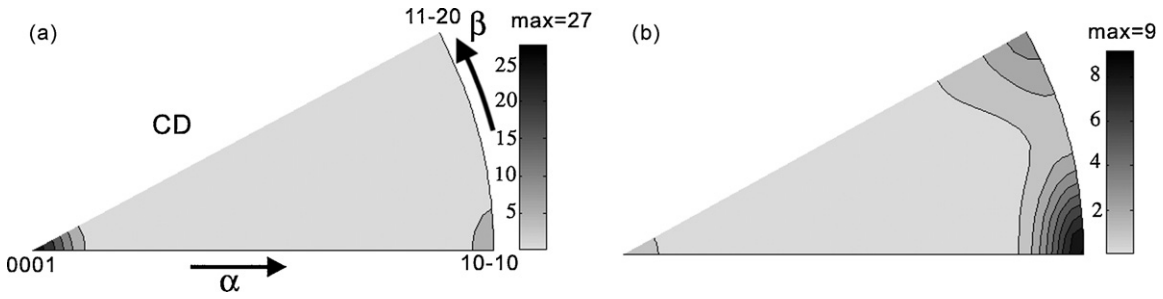


**Fig. 12.** Measured inverse pole figures showing the macroscopic texture development (with respect to tensile twinning) of CDED specimens at selected deformation temperatures. (a) $T = 300\,^{\circ}C$; (b) $T = 400\,^{\circ}C$. $\varepsilon = -0.15$, $\dot{\varepsilon} = 10^{-2}\,s^{-1}$.

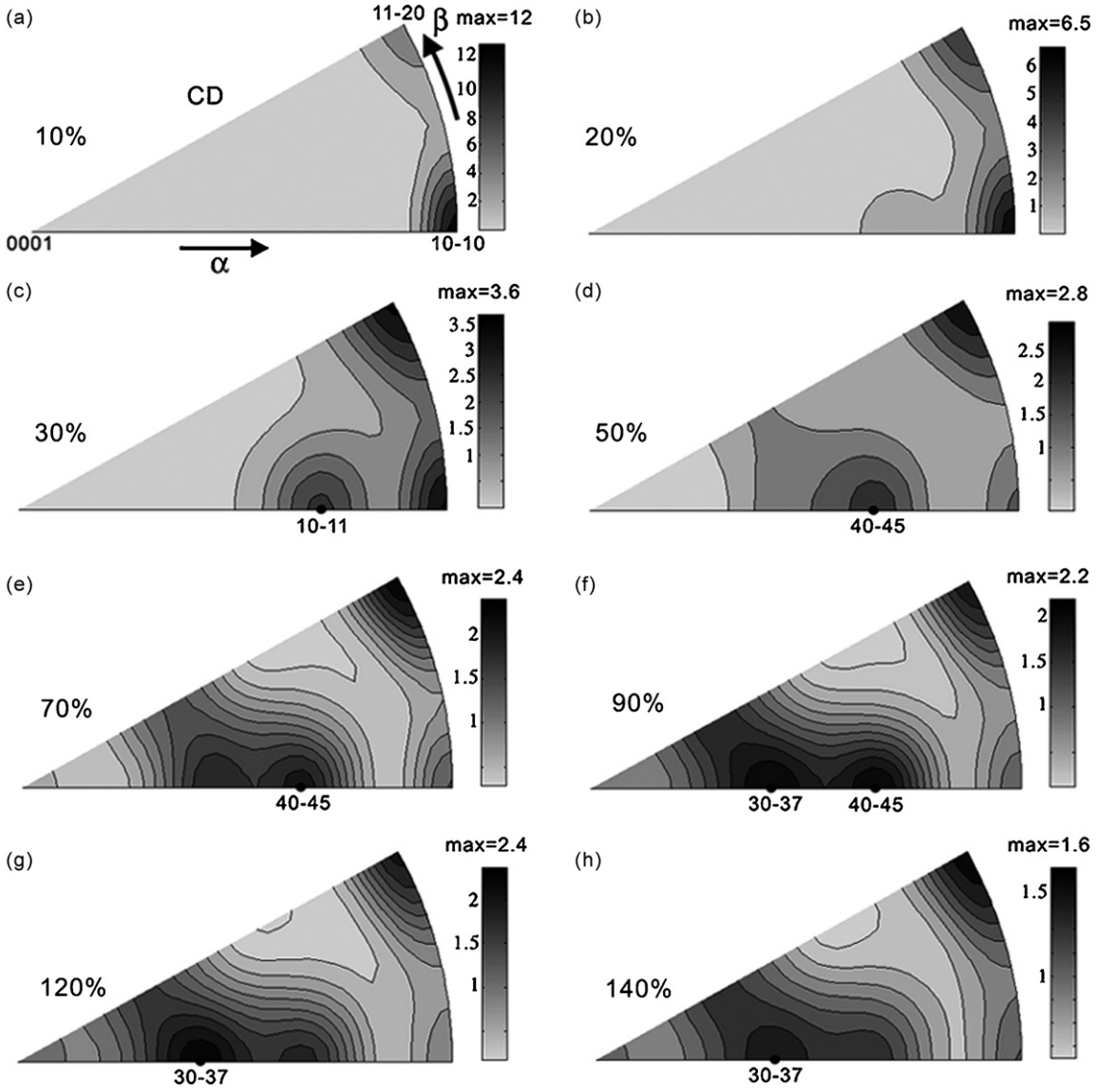


**Fig. 13.** Measured inverse pole figures showing the macroscopic texture development (with respect to texture randomization) of CDED specimens during compression at 400 °C/$10^{-4}$ $s^{-1}$ to selected final strains ranging from (a) $\varepsilon = -0.1$ to (h) $\varepsilon = -1.4$.

in the inverse pole figure, developing a $< 40\bar{4}5 >$ CD orientation, at intermediate strain levels (50% deformation) (Fig. 13d). Additionally, the peak intensity of the prismatic texture component at $\alpha = 90°$ shifts from $< 10\bar{1}0 >$ to $< 11\bar{2}0 >$ pole. During larger strains, i.e. between −50% and −140% basal slip remains a main deformation contributor, and the texture changes slightly, showing a transition from a $< 40\bar{4}5 >$ CD orientation, at ($\alpha = 57°$, $\beta = 0°$) to $< 30\bar{3}7 >$ CD orientation, at ($\alpha = 38°$, $\beta = 0°$) (Fig. 13e–h).

Tracking the change in texture strength in Fig. 13 reveals that under the current conditions there is a strong tendency for texture randomization. The texture intensity drops from 16 MRD prior to compression to less than 2 MRD after 140% deformation (cf. Fig. 1c and Fig. 13h). Note that the important changes in the texture development take place during incipient to intermediate stages of deformation. Already after 50% strain, the texture sharpness drops by more than 80%, and the strong starting orientation is replaced

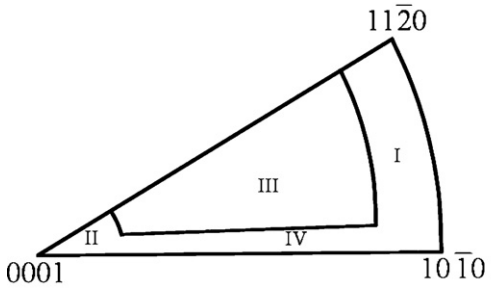


| | compression | tension |
|---|---|---|
| I | {10$\bar{1}$2} twinning, prismatic slip, <a> pyramidal slip | prismatic slip, <a> pyramidal slip |
| II | <c+a> pyramidal slip | {10$\bar{1}$2} twinning, <c+a> pyramidal slip |
| III | single basal slip | single basal slip |
| IV | double basal slip | double basal slip |

**Fig. 14.** Orientation dependence of active deformation mechanisms in magnesium [13].

by three weak orientations. The observed texture decay can be explained on the basis of (i) a higher glide activity at elevated temperatures due to the activation of additional slip systems and, therefore, a more homogeneous partitioning of slip to the participating slip systems (prismatic slip, <a> pyramidal slip and basal slip), which in turn promotes good ductility, reduces anisotropy and leads to a weak texture development (ii) DRX, which is known to counteract the strong deformation texture, and thus reduces the overall texture intensity of the material. A processing window of 400 °C/$10^{-4}$ $s^{-1}$ ensures a very active role for DRX.

For compression at 45° from ED (CD45ED specimens), the initial major texture component at $< 3\,0\,\bar{3}\,4 >$ pole can favorably deform by basal glide, and the minor texture components with the *c*-axes perpendicular to the loading axis are prone to twinning (Fig. 1d). At 200 °C/$10^{-2}$ $s^{-1}$ (highest *Z* condition) the resulting texture development shows a preferred basal orientation (basal planes aligned with the compression surface) (Fig. 7a), whereas at lower *Z* conditions (Fig. 7b–d) the texture is rotated by ~15° away from the <0 0 0 1> pole in the respective inverse pole figures. In terms of flow behavior, considerable variations are seen between the flow curve at 200 °C/$10^{-2}$ $s^{-1}$ (highest *Z* condition) and the curves obtained during lower *Z* deformation (Fig. 2d). When deforming at a relatively low temperature of 200 °C and a high strain rate of $10^{-2}$ $s^{-1}$ DRX is firstly postponed till a certain critical strain is reached, and the deformation is mainly controlled by basal slip. With shearing taking place on (0 0 0 1) basal planes, grains undergoing basal slip are gradually rotated away from their actual orientations into a basal orientation. During this process, the Schmid factor for basal slip progressively decreases, hence, hardening basal slip till it is eventually exhausted. This explains the flow behavior at 200 °C/$10^{-2}$ $s^{-1}$, where the stress–strain curve shows a wide strain hardening regime at a moderate slope prior to the onset of DRX. The flow curves at lower *Z* conditions (higher temperature and lower strain rates) depict virtually no work hardening after yielding and can be characterized by a steady-state flow. From the absence of a typical basal texture upon lower *Z* deformation, it can be concluded that the deformation was accommodated by a combination of basal slip and pyramidal <*c* + *a*> slip, that retained a final texture located between <0 0 0 1>CD and $< 1\,1\,\bar{2}\,2 >$ CD components.

### 4.2. Deformation behavior during tension

For tensile loading along the extrusion direction the initial prismatic texture behaves differently to the previous case of compression in resisting slip and favoring twinning. As aforementioned, $\{1\,0\,\bar{1}\,2\}$ -tensile twinning creates extension along the *c*-direction, and thus it cannot operate for tensile loads in the basal plane. Conversely, $\{10\bar{1}1\}$-compression twinning supports compression along the *c*-direction, and hence, it would be conceivable as a deformation mechanism in this particular case. Our findings, however, do not corroborate such an assumption. While compressive twins exist and have been occasionally linked to the initiation of fracture at temperatures below 150 °C [7,18], they are scarce and do not contribute much to plastic deformation. With respect to slip, the resolved shear stress on the basal slip systems is still, as in the case for compression close to zero, and the constraints of the limited number of independent slip systems cause a high yield and flow stress (Fig. 2a), with hardening consistent with a predominant prismatic <*a*> slip deformation. In fact, with a starting orientation such as $< 1\,0\,\bar{1}\,0 >$ TD, The Schmid factor is highest for prismatic planes ($m$ = 0.433) and the sample is suitably oriented for symmetric double prismatic slip with the resulting slip direction lying parallel to the tensile axis. In such case, accommodation of plastic strain comprises contraction in the $< 1\,0\,\bar{1}\,0 >$ directions and elongation in the $< 1\,1\,\bar{2}\,0 >$ directions, thus rendering the shape change maximum in the basal plane and equal to zero along the *c*-axis. This results in the orientation of individual grains remaining virtually unchanged during deformation (Fig. 4). Fig. 15 shows the Schmid factor maps for different slip systems, obtained by EBSD on a TDED tension specimen strained at 200 °C/$10^{-4}$ $s^{-1}$ to failure. Fig. 15c and f indicates that by the time failure occurred due to necking, the Schmid factor of deformed grains was still highest for prismatic slip. The microstructure was also somewhat suitably oriented for pyramidal <*c* + *a*> slip (Fig. 15b and e), but there were no indications in the texture development that this slip system was an important deformation contributor (not even for lower *Z* conditions). This is most likely because, in this particular case, strain accommodation along the *c*-direction was not necessary.

Tensile deformation in a direction inclined by 45° to the original extrusion direction is characterized by considerably lower yield stress as a result of basal slip activity (Fig. 2b). In Fig. 6 the pole distance $\alpha$, at which the peak intensity is located in the inverse pole figures, is directly related to the amount of shear initiated by basal slip. For straining at highest *Z* (200 °C/$10^{-2}$ $s^{-1}$), the peak position of the initial texture component $< 3\,0\,\bar{3}\,4 >$ ED (Fig. 1d) (suitably oriented for basal slip) moves by $\Delta\alpha \sim 10°$ from ($\alpha = 57°$, $\beta = 0°$) (initial orientation) to a new favorable orientation; $< 1\,0\,\bar{1}\,1 >$ TD at ($\alpha = 67°$, $\beta = 0°$) (Fig. 6a). Tension at lower *Z* conditions (higher temperature and/or lower strain rate) shows lower crystallographic reorientation of the starting texture relative to the previous case at highest *Z*. The initial texture component is shifted by $\Delta\alpha \sim 5°$, from ($\alpha = 57°$, $\beta = 0°$) to ($\alpha = 62°$, $\beta = 0°$); i.e. $< 3\,0\,\bar{3}\,4 >$ ED → $< 4\,0\,\bar{4}\,5 >$ TD(Fig. 6b–d). We can conclude that the amount of basal slip contribution to deformation at 200 °C/$10^{-2}$ $s^{-1}$ is higher than in other cases, in which additional slip systems and DRX play more important roles in the deformation. For tension at 200 °C/$10^{-2}$ $s^{-1}$ prismatic <*a*> slip seems to be also important to accommodate deformation in certain grains, where basal planes are aligned parallel to the tensile axis. This would explain the additional strong concentration of prismatic poles parallel to TD (Fig. 6a).

### 4.3. Characterization of dynamic recrystallization (DRX)

#### 4.3.1. DRX mechanisms

DRX in magnesium contributes to the relaxation of stress concentration caused by the lack of easily activated slip systems, and thus to the delay of premature failure and improving the ductility. Even though the flow curves for tension do not exhibit certain characteristics of a material undergoing DRX (i.e. peak flow behavior), the occurrence of DRX during tensile deformation was evident in the optical microstructure (Fig. 8b) upon straining at 200 °C/$10^{-2}$ $s^{-1}$ to failure. DRX in tension seems to proceed similarly as in compression by grain boundary nucleation followed by necklace formation [19,20]. The recrystallized grain size and volume fraction show strong dependency on the *Z* value, i.e. on the temperature and strain rate (Fig. 10). Indications of DRX during tension were also visible in the deformation texture development, where the texture strength became weaker with decreasing *Z* and a 30° <0 0 0 1> orientation relationship was observed between deformation texture components (also reported in [21]). Fig. 16 shows orientation imaging microscopy (OIM) maps collected by EBSD on a TDED specimen deformed to failure at 200 °C/$10^{-4}$ $s^{-1}$. The formation of fine DRX grains along grain boundaries of deformed grains is believed to occur by two different mechanisms:

(i) A discontinuous mechanism based on conventional nucleation of DRX by grain boundary bulging. Consistent with this mechanism, in which the growth of recrystallizing grains plays a major role, is the formation of serrated grain boundaries, particularly among the coarser grains, as shown in Fig. 16b. Serrated boundaries are thought to form when the density of dislocations

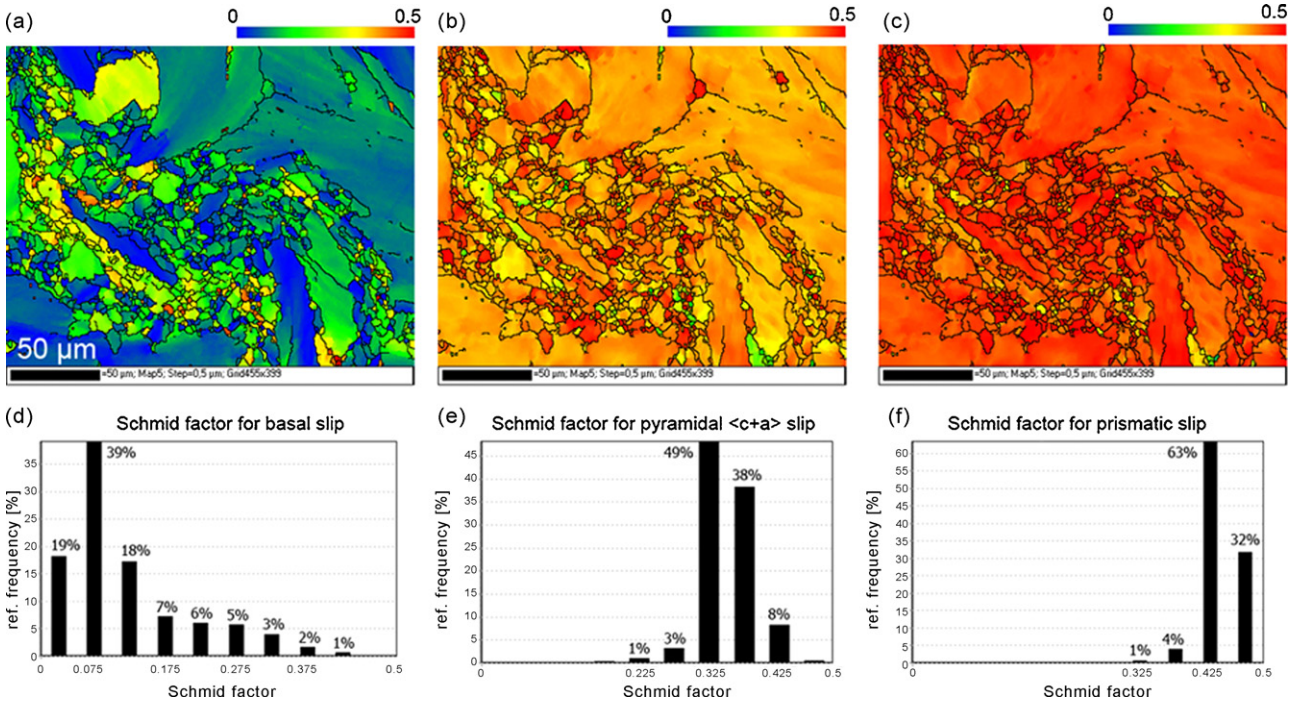


**Fig. 15.** Schmid factor (SF) distribution maps obtained by EBSD on TDED specimen tensiled at 200 °C/$10^{-4}$ $s^{-1}$ to failure. (a) and (d) SF distribution for basal slip; (b) and (e) for pyramidal <*c* + *a*> slip; (c) and (f) for prismatic <*a*> slip. The scale indicates the calculated SF value. Measured surface is perpendicular to the tensile axis. Step size 0.2 µm.

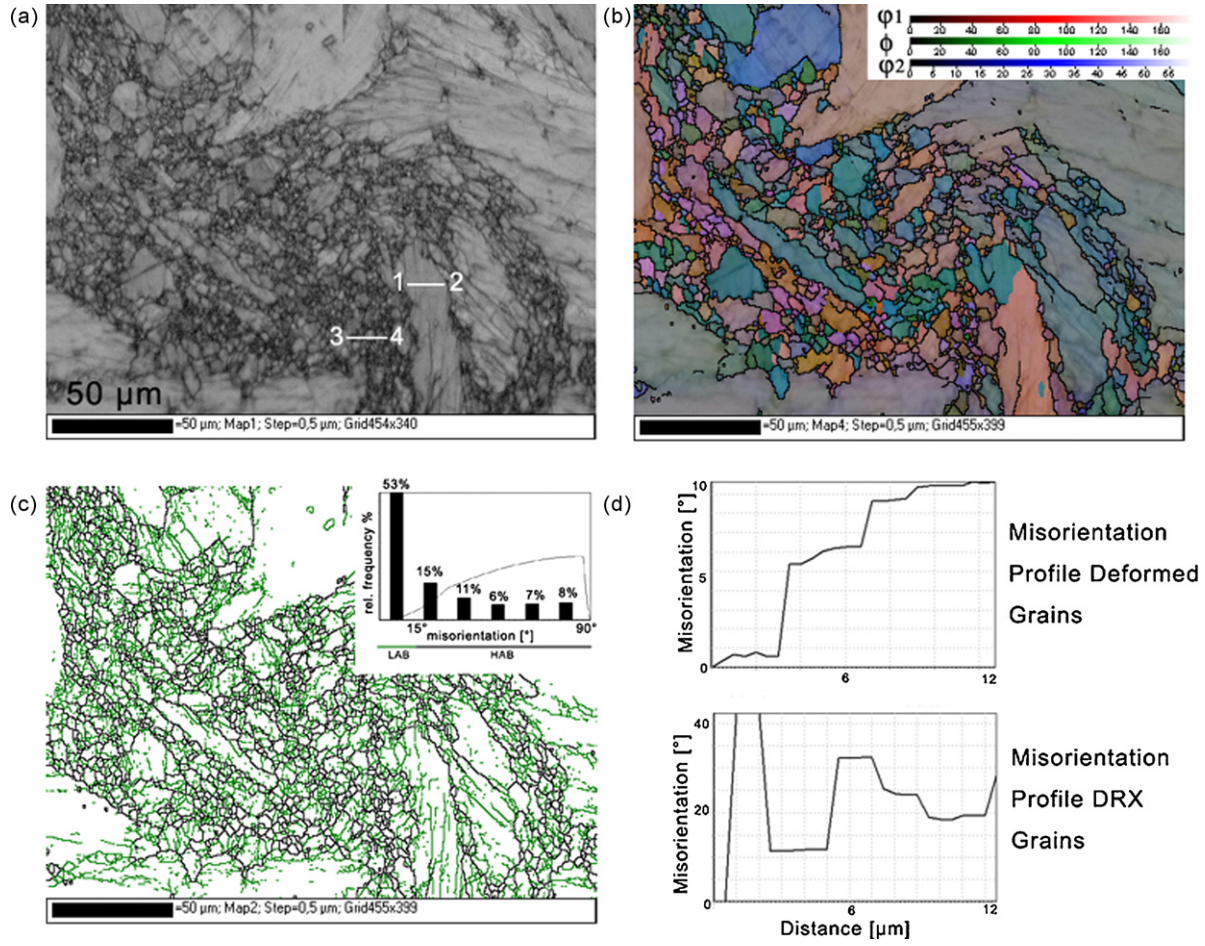


**Fig. 16.** OIM maps obtained by EBSD on TDED specimen tensiled at 200 °C/$10^{-4}$ $s^{-1}$ to failure. (a) Image quality map; (b) orientation map in terms of Euler angles; (c) grain boundary map; (d) misorientation profile within a deformed grain; (e) misorientation profile within a recrystallized region. Measured surface is perpendicular to the tensile axis. Step size is 0.2 µm.

entering grain boundaries exceeds their absorption capacity or when the absorption process necessitates an incubation time [22]. Owing to the fact that the coarser grains have larger grain boundary lengths, they will have a greater tendency to develop serrated grain boundaries (Fig. 16b). The process described here, i.e. the development of serrated grain boundaries of coarse grains and the nucleation of DRX by bulging, is of a discontinuous nature, and the sweeping action of formed high angle boundaries removes dislocations, resulting in strain free recrystallized grains.

(ii) A continuous mechanism which involves a gradual transformation of subgrain boundaries, particularly those near severely distorted boundary regions, into high angle boundaries including negligible amounts of boundary migration (frequently referred to as rotational dynamic recrystallization RDRX) [23–26]. Fig. 16d and e shows misorientation distributions within a deformed grain and a neighboring recrystallized region. For the deformed grain it is evident that the measured profile between point "1" close to the boundary, where DRX is observed and point "2" in the grain interior (cf. Fig. 16a) exhibits progressively increasing misorientations up to 10° (relative to the first point). The misorientation profile measured between points "3" and "4" (Fig. 16e) shows typical misorientation distribution behavior for a recrystallized region (i.e. alternating increase and decrease of misorientations upon crossing high angle boundaries).

Both mechanisms (i) and (ii) of grain boundary nucleation, lead to the formation of a necklace-type structure of fine recrystallized grains (*with high angle boundaries*) surrounding the former deformed grains, which obviously from Fig. 16c comprises a significant proportion of deformation induced subboundaries. Note that the observed 30° <0 0 0 1> orientation relationship between deformation and recrystallization texture components can only be attributed to discontinuous DRX because it necessitates grain boundary migration (nuclei with a 30° <0 0 0 1> misorientation relative to the deformed matrix are most favorable, and thus grow faster than other orientations).

### 4.3.2. Initiation of DRX

When DRX takes place, the stress–strain curve typically shows a behavior as illustrated in Fig. 2c, where an obvious stress peak is attained after initial work hardening. DRX, however, is initiated before the peak, at a critical stress $\sigma_c$ and a critical strain $\varepsilon_c$ (defined only for practical purposes since it is not a state parameter). Due to the progress of DRX, softening balances the continuing strain hardening in the unrecrystallized material. The balance is manifested by the peak stress $\sigma_p$. For determining the onset of DRX during compression, the strain at 80% of the peak stress $\sigma_p$ can be defined for practical purposes as the critical strain for the nucleation of DRX. On the other hand, when a stress-strain curve does not demonstrate a well-defined flow peak behavior, as in the present case of tension (Fig. 2a and b) other methods have to be deployed in order to determine the initiation of DRX. Jonas and co-workers [27–29] proposed that the onset of DRX corresponds to a local maximum in the stored deformation energy and a minimum in the dissipation rate, attained as a result of substructural evolution. Based on the equation $\partial/\partial\sigma = (-(\partial\theta_c/\partial\sigma)) = 0$ [28], the critical stress for DRX; $\sigma_c$ corresponds to the inflection point on the $\theta$–$\sigma$ curve as illustrated in Fig. 17a, where $\theta$ is the strain hardening rate; $\theta = \partial\sigma/\partial\varepsilon$. In other words, DRX begins when $\partial\theta/\partial\sigma$ reaches an extremum. On the contrary, a material not undergoing DRX will show a flow behavior as illustrated by the dashed line in Fig. 17a. Note that it is more accurate to use the inflection points in the $\theta$–$\sigma$ as an indication for DRX instead of looking at peaks in the stress–strain curves, as those inflection points would also appear even if no peak were visible. The same inflection point can also be detected by the minimum in the $-\partial\theta/\partial\sigma$ versus $\sigma$ curves (Fig. 17b). According to Fig. 17, the critical stresses for DRX at 200 °C/$10^{-2}$ $s^{-1}$ corresponding to specimen types TDED and TD45ED are equal to 146 MPa and 98 MPa, respectively. From Fig. 2a and b the respective strains for nucleation of DRX (as there is no critical strain for nucleus growth) are $\varepsilon_c^{TDED} = 0.04$ and $\varepsilon_c^{TD45ED} = 0.056$. This finding leads us to conclude that the nucleation of DRX in TDED specimens happens earlier than in the other specimen type, where tensile loading was applied at 45° inclination to the original extrusion axis. The accelerated onset of DRX in TDED specimens is most likely attributed to the higher hardening rate observed for their type, which is a manifestation of the active deformation mechanisms. As a reminder, the difference between the two sets of specimens lies in the fact that for one type (TDED) the deformation does not incorporate any shape change along the *c*-axis, and the macroscopic stress and strain are directly related to the shear stress and shear, whereas for the other type (TD45ED), straining along the *c*-axis is associated with a lattice rotation, and thus, a change of crystal orientation. There might be no direct line between the two straining scenarios and the onset of DRX, but for each scenario a different deformation mechanism is required, which in turn necessitates different activation stresses, and thus different stored energies in the form of dislocation substructures. It is noteworthy, that besides DRX other dissipation mechanisms, such like the initiation of twinning and microcracks can cause an inflection point in the $\theta$–$\sigma$ curves. In the present case (tension loading at 200 °C/$10^{-2}$ $s^{-1}$), both twinning and crack initiation can be safely ruled out, and the behavior discussed above remains solely confined to DRX.

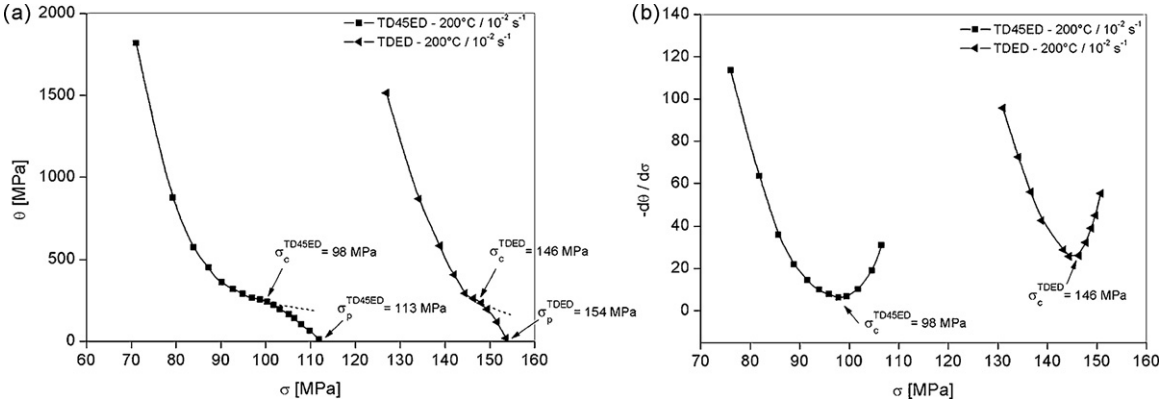


**Fig. 17.** (a) strain hardening rate ($\theta$) vs. stress ($\sigma$) curves; (b) $\partial\theta/\partial\sigma$ vs. $\sigma$ curves for TDED and TD45ED specimens deformed in tension at 200 °C/$10^{-2}$ $s^{-1}$.

## 5. Conclusions

(1) The tension–compression strength anisotropy in strongly textured AZ31 alloy is notably pronounced (i) during higher $Z$ deformation (lower $T$ and higher $\dot{\varepsilon}$), and (ii) for compression parallel to the extrusion direction ED. Loading at 45° inclined to ED yields an isotropic tension–compression strength response.
(2) In connection with the loading mode, the starting orientation and the deformation conditions, the deformed material witnesses various combinations of slip and twinning. Compression at 200 °C and 300 °C parallel to the extrusion axis favors tensile twinning over prismatic slip, which gives rise to high hardening rates. At 400 °C the deformation is carried out by a combination of prismatic slip, <*a*> pyramidal slip and basal slip. Conversely, tension along the same direction resists twinning and favors prismatic slip, irrespective of the investigated range of $Z$.
(3) Compressive twins were not evident during *c*-axis compression (neither during tension along ED, nor during advanced stages of compression, where a basal texture was present). Deformation by prismatic slip does not incorporate any shape change along the *c*-axis, and the macroscopic quantities are directly related to the slip parameters.
(4) Loading at 45° to the extrusion direction invokes basal slip in both tension and compression, and is characterized by considerably lower strength relative to loading parallel to ED. Therefore, it can be expected that both deformation modes will develop connatural textures. The only reason why the textures shown in Figs. 6 and 7 were different is because they were obtained at different strains.
(5) DRX in tension seems to proceed similarly as in compression by grain boundary nucleation followed by necklace formation. Grain boundary bulging of newly formed chains of fine DRX grains along former grain boundaries requires higher energies, which might not be available, and hence the formation of new fine grains is thought to occur continuously by means of gradual transformation of subgrain boundaries into high angle boundaries.
(6) Nucleation of DRX during tension depends on the loading direction, and hence, on the initial orientation. The critical strains for the onset of DRX at 200 °C/$10^{-2}$ $s^{-1}$ were determined from the inflection point in the $\theta$–$\sigma$ curves. DRX occurs earlier when the samples are loaded in the extrusion direction, most likely because it implicates higher deformation energies.
(7) Uniaxial compression at a low $Z$ condition (400 °C/$10^{-4}$ $s^{-1}$) yielded a desired texture degeneration, which was explained on the basis of a more homogeneous partitioning of slip systems that reduces anisotropy and enhanced DRX, which counteracts the strong deformation texture. Texture randomization in wrought magnesium is a key factor in solving its formability problem. It can be somehow achieved by alloy modification (i.e. adding rare earth metals for example). However Mg–RE alloys are still far from yet being commercial and the current study demonstrates that texture randomization of a *typical* (commercial) Mg alloy is possible just by choosing the optimum starting texture and deformation conditions, i.e. without any modification of the chemical composition.

## Acknowledgments

This work was funded by the Deutsche Forschungsgemeinschaft DFG under grant (GO 335/27). X. Li is grateful for the financial support of the CSC scholarship from China. S. Ghosh Chowdhury is grateful for the financial support of the Alexander von Humboldt (AvH) Foundation during his stay at IMM. The authors are grateful to Prof. Dr. G. Gottstein for his valuable comments.

## References

[1] F. Kaiser, J. Bohlen, D. Letzig, K.U. Kainer, Mater. Sci. Forum 419–422 (2003) 315.
[2] X.Y. Lou, M. Li, R.K. Boger, S.R. Agnew, R.H. Wagoner, IJP 23 (2007) 44.
[3] M.H. Yoo, Metall. Trans. A 12 (1981) 409.
[4] S. Kleiner, P.J. Uggowitzer, Mater. Sci. Eng. A 379 (2004) 258.
[5] Y.N. Wang, J.C. Huang, Acta Mater. 55 (2007) 897.
[6] H. Yoshinaga, R. Horiuchi, Trans. JIM 4 (1963) 134.
[7] T. Al-Samman, G. Gottstein, Mater. Sci. Eng. A 488 (2008) 406.
[8] R. Hielscher, H. Schaeben, J. Appl. Cryst. 41 (2008) 1024.
[9] D.S. Gelles, Acta Cryst. A28 (1972) 471.
[10] S.R. Agnew, O. Duygulu, IJP 21 (2005) 1161.
[11] M.R. Barnett, Z. Kheshavarz, A.G. Beer, D. Atwell, Acta Mater. 52 (2004) 5093.
[12] E.A. Calnan, C.J.B. Clews, Phil. Mag. 42 (1951) 919.
[13] I. Saxl, I. Haslingerová, J. Czechoslov, J. Phys. B 24 (1974) 1351.
[14] K.Y. Zhu, D. Chaubet, B. Bacroix, F. Brisset, Acta Mater. 53 (2005) 5131.
[15] R.K. Nadella, I. Samajdar, G. Gottstein, in: K.U. Kainer (Ed.), Proceedings of the 6th International Conference on Magnesium Alloys and their Applications, September, Wiley-VCH, Wolfsburg, Germany, 2003, p. 1052.
[16] R. Klar, K. Lücke, Z. Metallkde 59 (1968) 194.
[17] N. Munroe, X. Tan, H. Gu, Scripta Mater. 36 (1997) 1383.
[18] M.R. Barnett, Mater. Sci. Eng. A 464 (2007) 8.
[19] A. Galiyev, R. Kaibyshev, G. Gottstein, Acta Mater. 49 (2001) 1199.
[20] T. Al-Samman, G. Gottstein, Mater. Sci. Eng. A 490 (2008) 411.
[21] G. Gottstein, T. Al-Samman, Mater. Sci. Forum 495–497 (2005) 623.
[22] R.Z. Valiev, O.A. Kaibyshev, Sh.Kh. Khannanov, Phys. Status Solidi A52 (1979) 447.
[23] S.E. Ion, F.J. Humphreys, S.H. White, Acta Metall. 30 (1982) 1909.
[24] J.C. Tan, M.J. Tan, Mater. Sci. Eng. A 339 (2003) 81.
[25] X. Yang, H. Miura, T. Sakai, Mater. Trans. 44 (2003) 197.
[26] M.T. Pérez-Prado, J.A. del Valle, J.M. Contreras, O.A. Ruano, Scripta Mater. 50 (2004) 661.
[27] E. Poliak, J. Jonas, Acta Mater. 44 (1996) 127.
[28] E. Poliak, J. Jonas, ISIJ Int. 43 (2003) 684.
[29] A. Najafizadeh, J. Jonas, ISIJ Int. 46 (2006) 1679.